Texture and microstructural evolution in an Al-6061 alloy processed by high-pressure torsion

Abdelkader Khalfallah[1,2], Hiba Azzeddine[1, *], Thierry Baudin[3], François Brisset[3], Yi Huang[4,5], Terence G. Langdon[4]

[1] Laboratory of Materials and Renewable Energy, Faculty of Sciences, Mohamed Boudiaf University, 28000 M'sila, Algeria
[2] Laboratoire de Mathématiques et Physique Appliquées, École Normale Supérieure de Bousaada, 28001 Bousaada, Algeria.
[3] Université Paris-Saclay, CNRS, Institut de chimie moléculaire et des matériaux d'Orsay, 91405 Orsay, France
[4] Materials Research Group, Department of Mechanical Engineering, University of Southampton, Southampton SO17 1BJ, UK
[5] Department of Design and Engineering, Faculty of Science and Technology, Bournemouth University, Poole, Dorset BH12 5BB, UK

* Corresponding author: Pr. Hiba Azzeddine, hiba.azzeddine@univ-msila.dz

Abstract

A commercial Al-6061 alloy was processed by high-pressure torsion at room temperature over equivalent strains in the range of $\varepsilon_{eq} = 0 - 205$ and the evolutions of the microstructure, texture and mechanical properties were investigated using electron backscatter diffraction and Vickers microhardness measurements. The mean grain size decreased significantly from ~121±5 μm in the initial state to ~0.45±0.15 μm after a strain of $\varepsilon_{eq} = 205$ and this grain refinement occurred in three distinct stages. First, the grain size decreased and saturated in the strain range of $\varepsilon_{eq} = 0 - 4.2$ accompanied by the development of an *A*-fiber shear texture and an increase in the microhardness. Continuous and discontinuous dynamic recrystallization were the main mechanisms for this grain refinement. Second, the grain size increased and the texture changed to a *B*-fiber texture between $\varepsilon_{eq} = 4.2$ and 10.2 producing a drop in the microhardness, where this grain growth was attributed to a strain-induced grain boundary migration. The mean grain size decreased and saturated again over the strain range of $\varepsilon_{eq} = 10.2 - 205$ where there was a weak but stable texture and a microhardness evolution following a model of hardening without recovery. Finally, the separate contributions of grain size, dislocation and texture strengthening to the overall hardening behavior were critically examined.

Keywords: Aluminum alloy; EBSD; High-pressure torsion; Texture; Ultrafine grains

1. Introduction

Wrought aluminum alloys, notably the 6xxx series (Al-Mg-Si), are regularly used in the automotive industries, the construction sector and in aerospace engineering owing to their high weight-to-strength ratio, excellent thermal conductivity, good corrosion resistance and general formability [1, 2]. Nevertheless, the scientific community faces major challenges in developing novel materials having superior mechanical properties that match modern industrial demands for use in advanced structural and functional applications.

The mechanical properties of the numerous 6xxx alloys can be enhanced either by thermal treatments or by deformation processing. Thermal treatments can increase the mechanical characteristics at high temperatures via processes such as precipitation hardening where the strengthening originates from the blocking of dislocation glide by dispersed precipitate phase particles that are formed during artificial aging [3]. The precipitation sequence in the Al-Mg-Si alloys has been identified as: Supersaturated solid solution (SSS) → Guinier-Preston zone (GP zone) → metastable β″ → metastable β′→ stable β [4-6] and it was established that the metastable β′ phase can provide the highest strengthening effect [5]. However, in practice the sequence of precipitation tends to be more complex and it is not easily controlled since different metastable phases may precipitate simultaneously depending on the chemical composition (Mg/Si ratio) and the heat treatment conditions of temperature and duration [7-9]. In addition, the nature and structure of the various metastable phases, especially in the early stages of the sequence as with the GP zones, remain at least partially unknown due to limitations in the experimental techniques so that their contribution to the strengthening processing is not well-defined [10].

In practice, processing using severe plastic deformation (SPD) techniques such as equal-channel angular pressing (ECAP) [11], accumulative roll-bonding (ARB) [12] or high-pressure torsion (HPT) [13] are well-known procedures for improving the mechanical properties of bulk materials by producing ultrafine grains at the sub-micrometer or nanometer level [14]. At present, HPT processing has attracted more attention than other SPD techniques due to its ability to generate microstructures with both smaller grain sizes [15-17] and higher proportions of high-angle grain boundaries which become important in utilizing these materials in operations such as superplastic forming [18, 19]. All of these characteristics are important for achieving the future commercialization of these nanostructured metals [20]. In HPT processing, deformation is attained through torsional shear straining and the application of a high hydrostatic pressure, usually in the range of 1-6 GPa, to a thin disc held between two massive

anvils [13]. In practice, the hydrostatic pressure associated with HPT processing allows the material to deform at a high equivalent strain ($\varepsilon_{eq} \geq 1000$) without cracking [19, 21, 22].

Several reports are now available on the HPT processing of Al-6061 alloys [23-29] but they generally deal with the effect of the strain induced by HPT on the precipitation kinetics of the alloy in order to achieve a beneficial and concomitant increase in the strength and ductility of the alloy [27-29]. The results reveal that HPT processing modifies the precipitation sequence and may significantly accelerate the precipitation kinetics due to the high density of dislocations and vacancies introduced by the processing. Indeed, these dislocations were considered responsible for the partial dissolution of the metastable β″ phase and its shape modification [29].

Nevertheless, only limited research is at present available focusing on the grain structure, texture and microhardness evolution of the commercial Al-6061 alloy subjected to HPT processing [23-26]. For example, a saturation in the average grain size of ~250 nm and a Vickers microhardness of ~155 Hv were recorded at equivalent strains above ~100 for the HPT-processing of the Al–0.6% Mg–0.4% Si (wt.%) alloy [25]. By contrast, the origins of the grain fragmentation, the texture development and more crucially their contributions to the material strengthening have not been sufficiently examined for the Al–Mg–Si alloys. Accordingly, the aim of the present research was to evaluate the impact of the strain induced by HPT processing on the grain refinement mechanisms, the dislocation density and the associated texture evolution in a commercial Al-6061 alloy. The alloy was processed by HPT at room temperature (RT) through an equivalent strain range of $\varepsilon_{eq} = 0 - 205$ and electron backscatter diffraction (EBSD) analyses and Vickers microhardness measurements were undertaken to provide metallurgical and mechanical characterizations, respectively.

2. Experimental materials and procedures

A commercial Al-6061 alloy was used in this investigation with a chemical composition in wt.% of 0.6% Mg, 1.4% Si, 0.17% Fe, 0.02% Cu with the remainder as Al.

The HPT processing was conducted on discs with diameters of 10 mm and thicknesses of $h \approx$ 0.85 mm at RT for numbers of revolutions N = 1/2, 2 and 10 turns under quasi-constrained conditions [30, 31]. The disc samples were processed at a pressure of 6.0 GPa with a rotation speed of 1 rpm. Attention was taken throughout the HPT processing to avoid the occurrence of slippage between the sample and anvils [32]. In practice, the temperature that arises during HPT

processing is very limited, which is believed to not significantly affect the microstructure and texture evolution [33, 34].

The microstructure, texture and microhardness measurements were performed near the centre ($r \approx 0.2$ mm), at the mid-radius position ($r \approx 2.5$ mm) and near the edge ($r \approx 4.8$ mm) on the horizonal cross-sections (the SD-RD plane) of the HPT-processed discs as illustrated in Figure 1. The shear reference frame was defined as the radial direction (RD), compression direction (CD) and shear direction (SD) as used earlier [35].

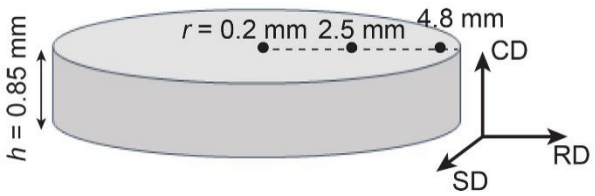

Figure 1: Location of the EBSD and microhardness measurements on the horizontal cross-section of the HPT disc, where SD, CD and RD define the coordinate system.

The results in this report are presented as a function of the equivalent strain, ε_{eq}, imposed by the HPT processing which is defined as [36]:

$$\varepsilon_{eq} = \frac{2\pi N r}{\sqrt{3}h} \quad (1)$$

The EBSD measurements were conducted using a TSL-EDAX-Hikari system mounted on a scanning electron microscope (FEG-SEM Zeiss Supra 55 VP) operating at 20 kV. The scanned area for the initial state ($N = 0$) was 2240 × 5120 μm^2 with a step size of 5 μm while the scanned areas for the HPT-processed discs were 50 × 50 μm^2 with a step size of 50 nm. The EBSD data were analysed using the Orientation Imaging Microscopy OIM^{TM} software. The average grain sizes were calculated from grain numbers ranging from 12458 to 187442 grains within the EBSD areas.

Grain boundaries with misorientation angles $\theta < 2°$ were excluded from the EBSD maps to prevent spurious boundaries due to orientation noise [37]. In this study, the grain boundaries were classified into the three types of very low-angle grain boundaries (VLAGBs) with misorientations $2° < \theta < 5°$, low-angle grain boundaries (LAGBs) with $5° < \theta < 15°$ and high-angle grain boundaries (HAGBs) with $\theta > 15°$, respectively.

The dislocation density, ρ_{GND}, from the geometrically necessary dislocations (GND) were estimated using the kernel average misorientation (KAM) approach following the equation [38, 39]:

$$\rho_{GND} = \frac{\alpha\theta_{KAM}}{n\delta b} \quad (2)$$

where α = 3 for grain boundaries with mixed character [40], δ is the EBSD scan step size, n corresponds to the nearest neighbor which defines the size of the kernel, θ_{KAM} is the average misorientation angle and b = 0.28 nm is the Burgers vector. The value of θ_{KAM} was calculated from the mean misorientation angle between a given point and its 3rd neighbor (n = 3) and by excluding misorientations of θ > 5°.

The proportion of dynamic recrystallization (DRX) was measured using the grain orientation spread (GOS) approach where grains with GOS < 1° are considered as free of dislocations and hence entirely recrystallized [41].

The resultant texture was analysed using toolbox MTEX by calculating the orientation distribution function (ODF) using the harmonic method (L = 22) and a Gaussian function with a half-width of 5° to model each orientation [42]. It is known that the shear deformation texture during HPT processing of Al alloys is weak and unstable [35] and hence it is preferable to use orthorhombic symmetry for the ODF calculations.

A SHIMADZU type HMV-2 tester was used to measure the Vickers microhardness of the disc samples. An average hardness value was calculated using at least three indentations with a load of 100 g and a dwell duration of 10 s.

3. Experimental results

The evolution of microstructure in the HPT-processed Al-6061 alloy through the various equivalent strains is depicted in Figure 2 using inverse pole figure (IPF) maps with respect to the CD direction with the color-coding depicted in the standard stereographic triangle. The initial state exhibits an equiaxed microstructure with a mean grain size of ~121±5 μm. Figure 2b shows that the initial grains are subdivided into disoriented regions after HPT processing at ε_{eq}= 0.2 indicating the occurrence of grain fragmentation. The black zone in the IPF maps denotes a no index region which may be due to the imposed microstructural distortion. A substantial change in the grain morphology and orientation is visible in the disc HPT-processed at ε_{eq}= 10.2 (Figure 2c). The microstructure is more homogenously distributed and formed of fine equiaxed grains reflecting an ultrafine microstructural development. Similar

microstructural characteristics are observed in the discs HPT-processed at ε_{eq}= 41 (Figure 2d) and ε_{eq}= 205 (Figure 2e) thereby indicating a saturation behavior.

Figure 3 displays the variation in the mean grain size, the HAGBs fraction, the DRX fraction and the GND dislocation density as a function of the equivalent strain of the HPT-processed Al-6061 alloy. The mean grain size of the initial state (~121±5 µm) rapidly decreased to ~0.46±0.09 µm at a strain of ε_{eq}= 0.8 and remained at this value to a strain of $\varepsilon_{eq} \approx 4.2$. Thereafter, it is apparent that the mean grain size increased with increasing strain to reach a value of ~0.73±0.08 µm at ε_{eq}= 10.2 and then started to decrease again with further strain to reach a saturation value of ~0.45 ±0.15 µm at a strain of $\varepsilon_{eq} \approx 205$.

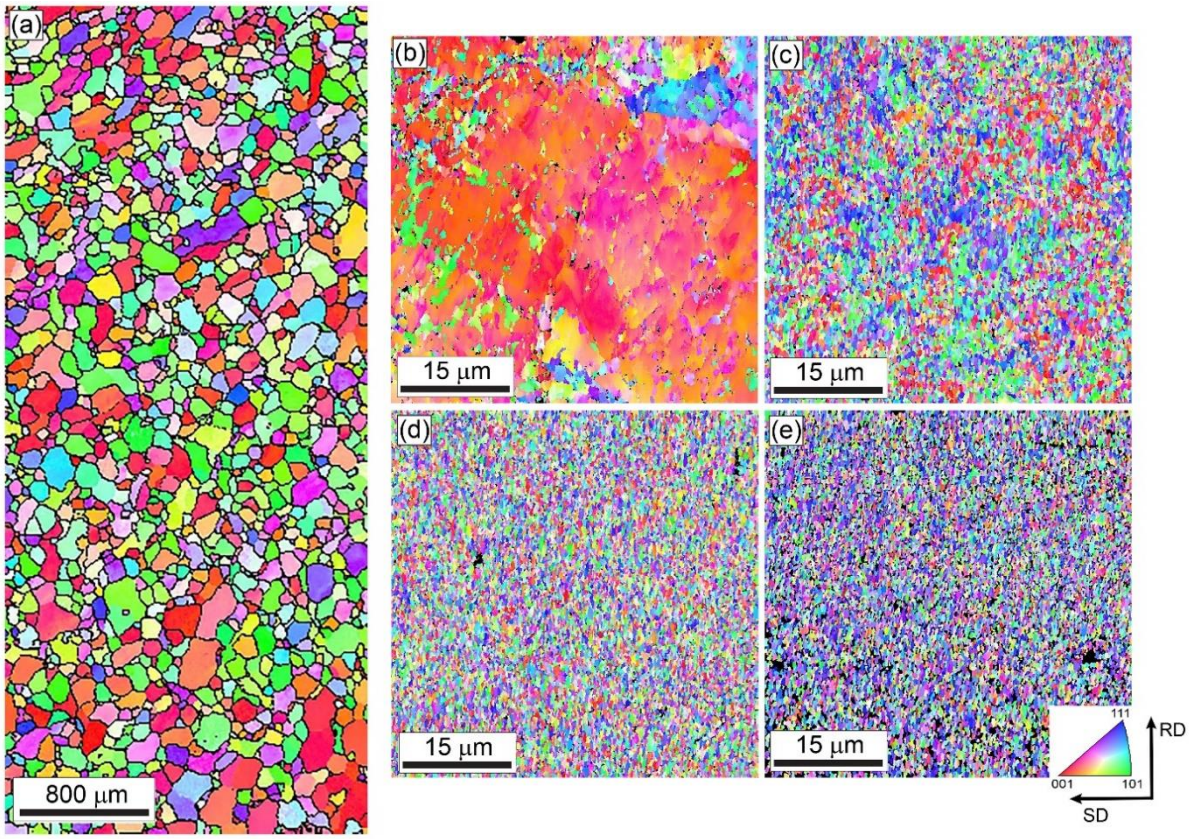

Figure 2: CD-IPF EBSD maps. Microstructure evolution of Al-6061 alloy after HPT processing through: (a) $\varepsilon_{eq} = 0$, (b) $\varepsilon_{eq} = 0.2$, (c) $\varepsilon_{eq} = 10.2$, (d) $\varepsilon_{eq} = 41$ and (e) $\varepsilon_{eq} = 205$.

The variation of the HAGBs (F_{HAGB}) and the DRX (F_{DRX}) fractions as a function of the equivalent strain share the same behavior. First, the HAGBs and DRX values decrease from $F_{HAGB} \approx 55\%$ and $F_{DRX} \approx 59\%$ in the initial state to $F_{HAGB} \approx 22\%$ and $F_{DRX} \approx 2\%$ after a strain of $\varepsilon_{eq} \approx 0.2$ due to the deformation process. Their values increased with increasing strain to reach values of $F_{HAGB} \approx 68.2\%$ and $F_{DRX} \approx 37.5\%$ after a strain of $\varepsilon_{eq} \approx 4.2$. Then the HAGBs

and DRX fractions decrease and there is an apparent steady-state situation between the strain ranges of $\varepsilon_{eq} \approx 5.3 - 21.3$. Finally, their values increase continuously with further strain to reach $F_{HAGB} \approx 77\%$ and $F_{DRX} \approx 57\%$ at a strain of $\varepsilon_{eq} \approx 205$.

Regarding the GND dislocation density, it increases to $\rho_{GND} \approx 1.96 \times 10^{15}$ m^{-2} after a strain of $\varepsilon_{eq} \approx 0.8$, and decreases to $\rho_{GND} \approx 1.69 \times 10^{15}$ m^{-2} after a strain of $\varepsilon_{eq} \approx 4.2$. The variation of ρ_{GND} between $\varepsilon_{eq} \approx 4.2$ and 10.2 is barely visible but there is a slow increase and then a maximum of 2.69×10^{15} m^{-2} after a strain of $\varepsilon_{eq} \approx 21.3$ before gradually decreasing to $\rho_{GND} \approx 1.26 \times 10^{15}$ m^{-2} at a strain of $\varepsilon_{eq} \approx 205$.

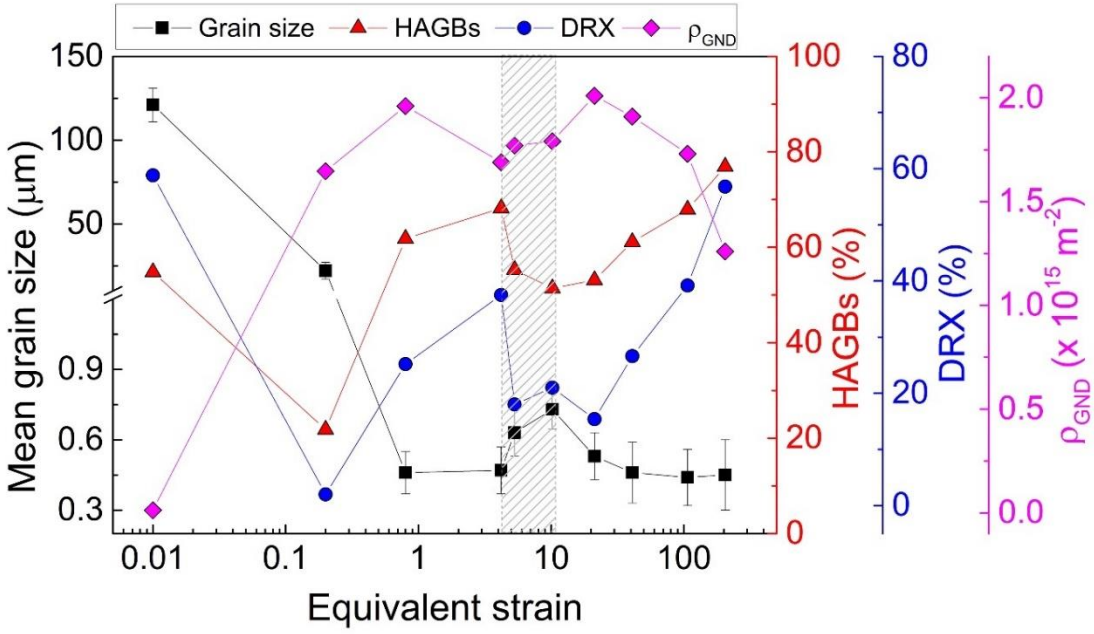

Figure 3: Evolution of mean grain size, HAGBs fraction, DRX fraction and GND ρ_{GND} density as a function of equivalent strain for the HPT-processed Al-6061 alloy.

The texture of the initial state and after HPT processing of the Al-6061 alloy is shown in Figure 4 in the form of ODF sections at $\varphi_2 = 0$ and 45°. The description and the ideal positions of the shear [35] and rolling texture components for materials with an FCC structure are summarized in Table 1 and Figure 4f. The shear texture is characterized by the formation of two fibers: an A-fiber containing $A, \bar{A}, A_1^*$ and A_2^* components (as shown by the black line in Figure 4f) and a B-fiber containing $A, \bar{A}, B, \bar{B}$ and C components (given by the blue line in Figure 4f) [35]. The volume fractions of the Brass, Goss, Cube, $A/\bar{A}$, A_1^*/A_2^*, $B/\bar{B}$ and C components as a function of equivalent strain are shown in Figures 5a and 5b, respectively. It is noted that the A, A_1^*,and

B components are equivalent to the $\bar{A}$, A_2^* and $\bar{B}$ components, respectively, since the ODF was calculated by assuming an orthorhombic sample symmetry.

Table 1. Ideal positions of shear and rolling texture components for FCC materials [35].

Shear texture			**Rolling texture**		
Notation	Miller indice {hkl}<uvw>	Euler angles (°) (φ_1, Φ, φ_2)	Notation	Miller indice {hkl}<uvw>	Euler angles (°) (φ_1, Φ, φ_2)
$\boldsymbol{A}$	{111}<110>	(60, 54.7, 45)	**Brass (Bs)**	{011}<211>	(35, 45, 0)
$\boldsymbol{\bar{A}}$	{111}<110>	(120, 54.7, 45)	**Goss (G_1)**	{011}<100>	(0, 45, 0)
$\boldsymbol{A_1^*}$	{111}<112>	(90, 54.7, 45)	**Rotated Goss (G_2)**	{011}<011>	(90, 45, 0)
$\boldsymbol{A_2^*}$	{111}<211>	(30, 54.7, 45)	**Cube (Cu)**	{001}<100>	(0, 0, 0)
B	$\{1\bar{1}2\}$<110>	(50.7, 65.9, 63.4)			
$\boldsymbol{\bar{B}}$	$\{\bar{1}1\bar{2}\}$<11$\bar{1}$0>	(0, 35.26, 45)			
$\boldsymbol{C}$	{001}<110>	(45, 0, 0)			

The initial state exhibits the presence of recrystallization texture components such as Cube (Cu), near Goss (G_1) and rotated Goss (G_2) and a retained Brass (Bs) deformation texture component which is a typical texture for sheet Al-based alloys [37, 43].

The ODF sections of the disc which was HPT-processed at $\varepsilon_{eq} = 0.2$ indicate the domination of the Cube texture components. This is expected since the IPF map (Figure 2b) contains a limited number of grains.

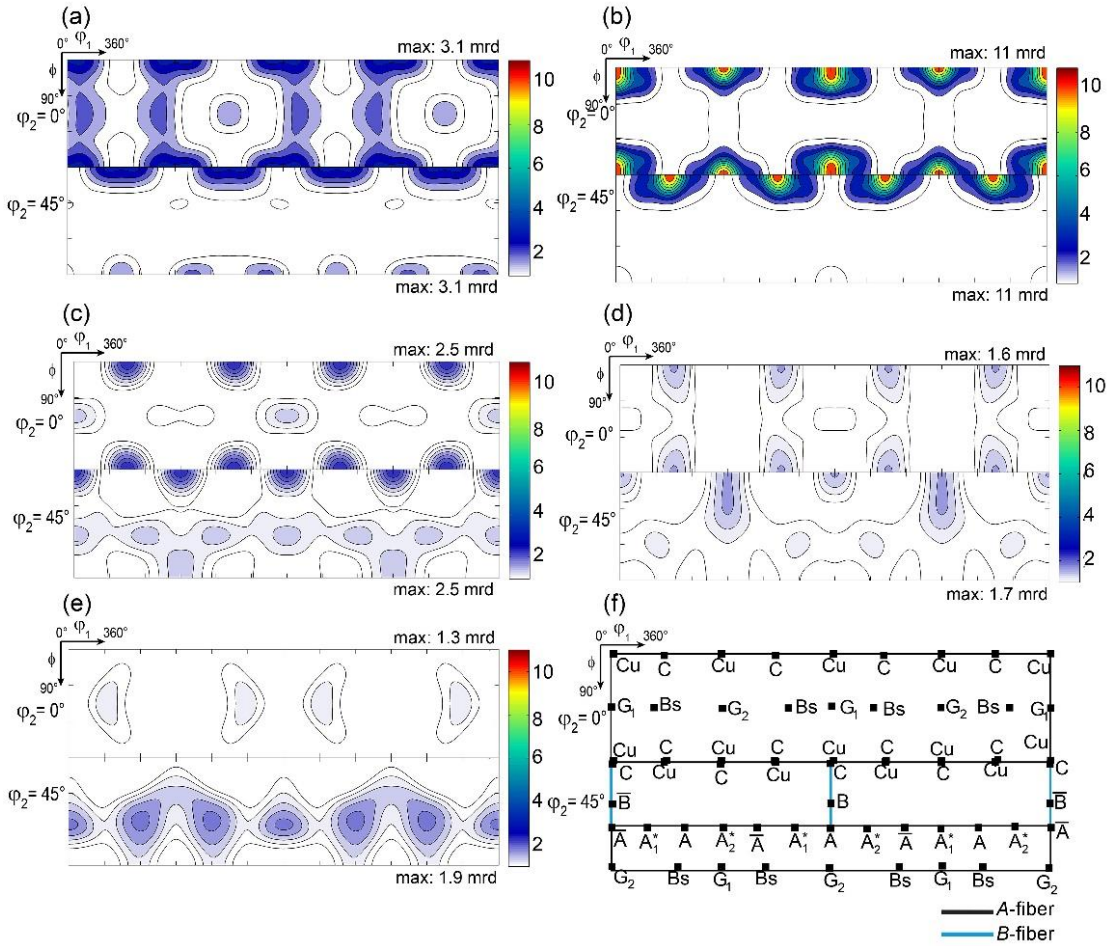

Figure 4: ODF sections at φ_2 = 0 and 45° of A-l6061 alloy processed at: (a) ε_{eq} = 0, (b) ε_{eq} = 0.2, (c) ε_{eq} = 10.2, (d) ε_{eq} = 41 and (e) ε_{eq} = 205. (f) ODF sections at φ_2 = 0 and 45° displaying the positions of the ideal shear and rolling texture for materials with FCC structure.

As can be seen from Figure 5b, a shear texture type appeared after processing at ε_{eq} = 0.8, where the fraction of A_1^*/A_2^* components is the highest followed by the $A/\bar{A}$ components, indicating the dominance of the *A*-fiber. The *A*-fiber texture remains stable until a strain of ε_{eq} = 4.2. Thereafter the fractions of $B/\bar{B}$ and $A/\bar{A}$ components increase significantly after a strain of ε_{eq} = 5.3 leading to the development of a *B*-fiber with the dominance of $B/\bar{B}$ components. At this stage, the Brass component also increases strongly. However, this shear texture type changes again after a strain of ε_{eq} = 10.2.

It is apparent from the ODF sections in Figure 4c and demonstrated in Figure 5b that the *C*, $A/\bar{A}$, A_1^*/A_2^*, and $B/\bar{B}$ components are all present with similar volume fraction. The shear texture becomes weaker and tends to be stable with increasing strain up to ε_{eq} = 205. It is interesting to note that the Brass component remains present even after the high shear strain of ε_{eq} = 205.

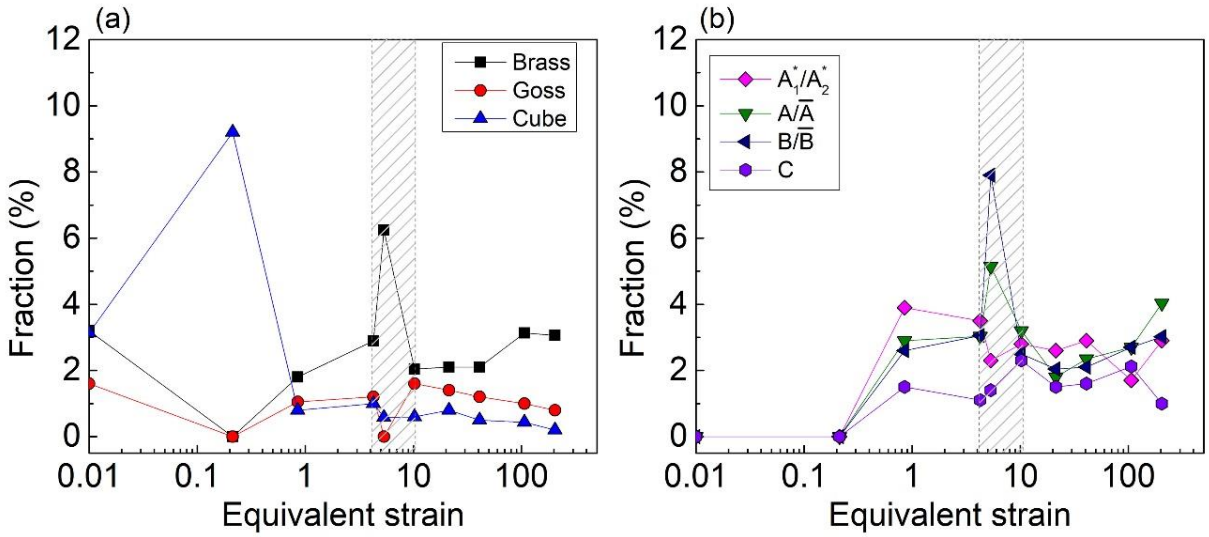

Figure 5: Evolution of: (a) rolling (Brass, Goss and Cube) and (b) shear texture ($A/\bar{A}$, A_1^*/A_2^*, $B/\bar{B}$ and C) components as a function of equivalent strain for HPT-processed Al-6061 alloy.

The evolution of microhardness (Hv) as a function of the equivalent strain is shown in Figure 6. The Hv value increases from ~102±3 Hv in the initial state to ~148±2 Hv after HPT processing at ε_{eq} = 4.2. There is a noticeable decrease in the Hv value at ε_{eq} = 5.3 (~133±3 Hv), and then it rises again with increasing strain to reach a maximum value of ~155±3 Hv at ε_{eq} = 40.9 and tends to saturate with further strain up to ε_{eq} = 205.

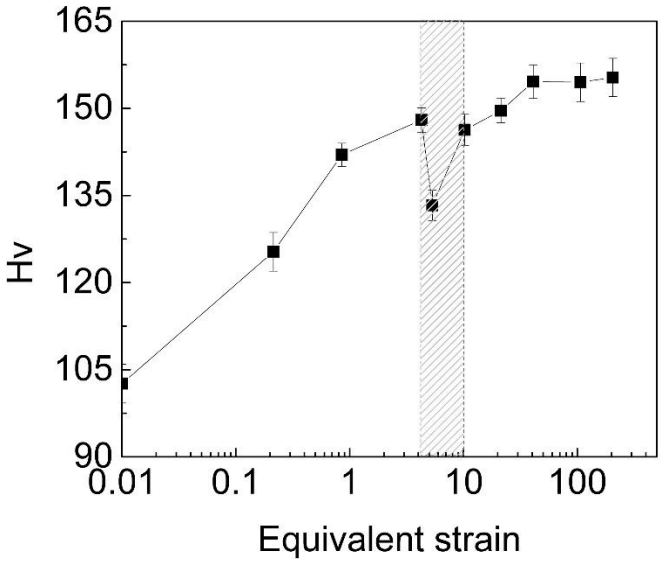

Figure 6: Microhardness evolution as a function of equivalent strain for the HPT-processed Al-6061 alloy.

4. Discussion

4.1 Microstructural characteristics of the Al-6061 alloy in HPT processing

Generally, the grain refinement mechanism for materials with medium to high stacking fault energy (SFE), such as Al-6061 alloy where the SFE is $\gamma_{SFE} \approx 150$ mJ/m^2 [44], can be divided into two distinct parts: grain fragmentation and a steady-state region [45]. Accordingly, the microstructural parameter evolution through the equivalent strain of the HPT-processed Al-6061 alloy as shown in Figure 3 provides clear evidence that the alloy goes through two grain refinement stages. The first stage is where the grain size decreases and saturates in the strain range of $\varepsilon_{eq} = 0 - 4.2$, and then the second stage occurs over the strain range of $\varepsilon_{eq} = 10.2 - 205$. Indeed, Figure 3 shows that the mean grain size coarsens between a strain of $\varepsilon_{eq} = 4.2$ and 10.2 thereby allowing the second stage of grain refinement to take place.

Figure 7 shows interesting deformation features that occurred in the HPT discs processed at the first grain fragmentation part ($\varepsilon_{eq} = 0.2$), the first saturation part ($\varepsilon_{eq} = 4.2$) and Figure 8 at the second fragmentation part ($\varepsilon_{eq} = 10.2$). The microstructures are presented by CD-IPF maps superimposed by the grain boundary type: VLAGBs, LAGBs and HAGBs, and GOS and KAM maps. The evolution of VLAGBs, LAGBs and HAGBs in the three regions are summarized in Table 2.

The first deformation feature can be noted from Figures 7a-c. Figure 7a and the magnification of the black frame (Figure 7d) is evidence for the formation of elongated bands in the Cube oriented grains (red color) delimited by LAGBs and surrounded by a high fraction of VLAGBs which causes the formation of an orientation gradient within the parent grain as demonstrated by the gradual increase in the misorientation angle profile from points A to B in Figure 7e. Table 2 indicates a high fraction of VLAGBs which result from the generation of dislocations. The KAM map in Figure 7b shows the existence of high deformation distortion that originated from the GND densities located within the grains and also along the grain boundaries. Small dynamically recrystallized grains start to form inside the deformed grains as indicated by the white arrows in the GOS map (Figure 7c), thus indicating the occurrence of a continuous DRX (CDRX) mechanism [46]. The continuous generation of dislocations and their high mobility lead to their accumulation to form sub-grain boundaries (VLAGBs) and progressively transform to LAGBs and then to HAGBs [46]. Eventually, the dislocation density decreases, and the fraction of dynamically recrystallized grains or new grains increases with further strain, as is evident by the evolution of the ρ_{GND}, HAGBs and DRX fractions between strains of ε_{eq}= 0.8 and 4.2 in Figure 3.

The second noticeable deformation feature is the serration of the original grain boundary as in Figures 7a and d where this indicates the occurrence of a discontinuous DRX (DDRX) mechanism generally known as the strain-induced boundary migration (SIBM) mechanism [46]. The serration and bulging of the grain boundaries originate from the differences in the dislocation densities between both sides of the grain boundaries, as is evident from the increase in the misorientation profile of the CD distance in Figure 7e. Thus, the misorientation around the grain boundaries increases with further strain leading to the nucleation and formation of new grains [46]. It is evident from inspection of the GOS map in Figure 7c that small dynamically recrystallized grains, marked in blue, start to nucleate along the grain boundary as indicated by the black arrows. It appears that the CDRX mechanism is the primary grain refinement mechanism for materials with medium to high SFE where the deformation is accommodated by the activation of dislocation slip systems [46, 47]. Nevertheless, the present results show that the CDRX and DDRX mechanisms operated simultaneously and are the main processes for achieving grain refinement in the HPT-processed Al-6061 alloy.

At this stage of fragmentation, the shear texture has not been formed but the orientations of the small DRX grains formed by CDRX or DDRX are different from the parent grain which has Cube orientation. As shown in Figure 5b, a typical shear texture was developed at a strain of ε_{eq} = 0.85 and remained stable up to a strain of ε_{eq} = 4.2.

The microstructure at the steady-state stage of the disc processed at ε_{eq}= 4.2 is shown in Figures 7f and 7g. For this condition, the microstructure is homogenously distributed and it is characterized by typical equiaxed grains and a relative high fraction of HAGBs (~67.8%) as indicated in Table 2. The grains are mostly free of deformation as demonstrated by the GOS map where the majority of grains have no dislocations (blue color) which explains the decrease in the GND density noted in Figure 3. There was a mean saturated grain size of ~ 0.47 ± 0.1 µm between a strain of ε_{eq} = 0.8 and 4.2. Usually a saturation in the mean grain size is also accompanied by a saturation in the microhardness value but during the first grain refinement, between strains of ε_{eq} = 0 and 4.2, the microhardness increases and does not saturate as shown in Figure 6. Therefore, it is reasonable to conclude that a fully stable ultrafine microstructure was not attained in this research.

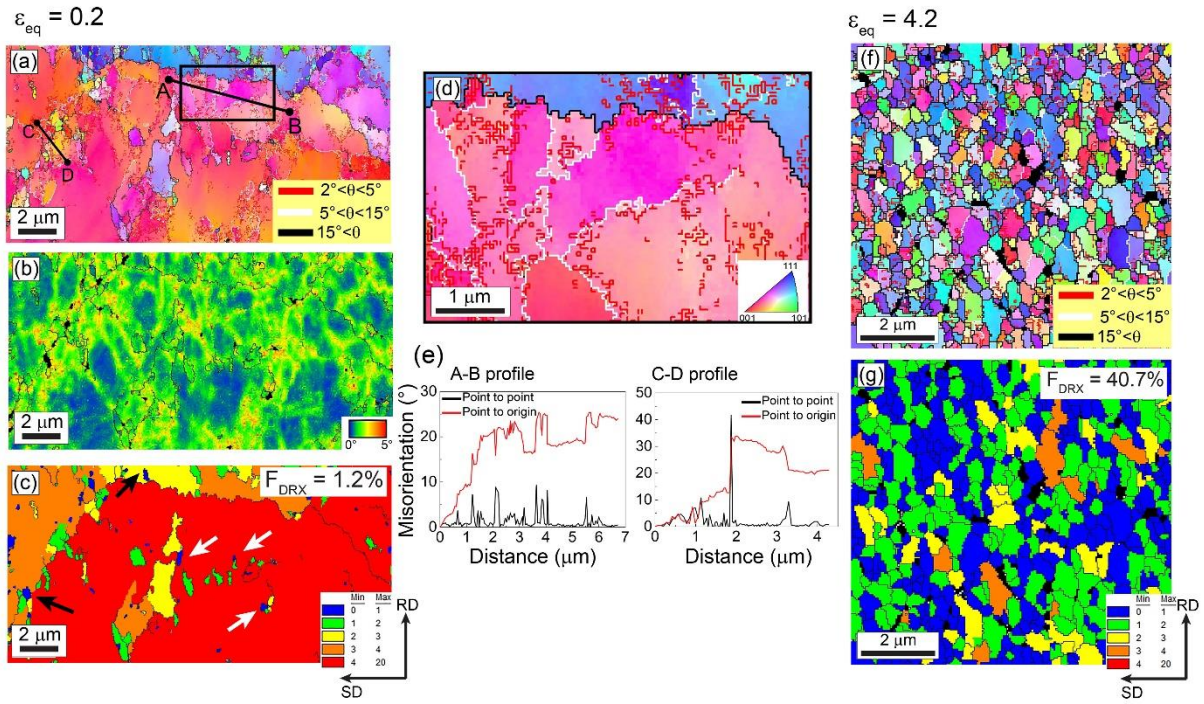

Figure 7: (a) CD-IPF map superimposed with grain boundary type (VLAGBs, LAGBs and HAGBs), (b) KAM, (c) GOS maps of a selected region from the disc processed at ε_{eq} = 0.2 (from Figure 2b), (d) CD-IPF map of the zoom of the black frame shown in Figure 7a and (e) misorientation profiles along AB and CD distances indicated in Figure 7a, (f) CD-IPF map superimposed with grain boundary type and (g) GOS map of region from HPT-disc processed at ε_{eq} = 4.2.

Table 2. Fraction of VLAGBs, LAGBs and HAGBs present in zones shown in Figures 7a, 7f and 8a.

ε_{eq}	0.2	4.2	10.2
VLAGBs (%)	57.1	25.3	33.8
LAGBs (%)	18.2	6.9	14.9
HAGBs (%)	24.7	67.8	51.4

Indeed, after HPT processing at the strain of ε_{eq} = 10.2 in Figure 8a, the microstructure becomes more heterogeneous and consists of a mixture of equiaxed and large elongated grains. The GOS map in Figure 8b demonstrates that the elongated grains are highly distorted because they contain high fractions of VLAGBs and LAGBs as in Figure 8a. At this stage of the deformation, the fractions of VLAGBs and LAGBs rise again while the fraction of HAGBs drops, as shown in Table 2, due to the generation of additional dislocations. The density of dislocations increases up to the strain of ε_{eq} = 21.3 before decreasing during the second steady-state phase, as indicated in Figure 3. Simultaneously, the HAGBs and DRX fractions increase during the steady-state

phase. It is interesting to note that both of these grain refinement stages reached similar grain sizes at the saturated stage, corresponding to ~0.47±0.1 µm at ε_{eq} = 4.2 and ~0.45±0.15 µm at ε_{eq} = 205. This suggests that there is effectively a critical limit in reducing the grain size through HPT processing. It was found earlier that HPT processing can refine the microstructure of the Al-6061 alloy in the range of ~0.25 – 0.40 µm above a strain of 100 depending on the initial state of the alloy [25, 26]. In the present investigation, the steady-state of the second grain refinement was accompanied by a saturation of the microhardness values as shown in see Figure 6. However, it was established in a very recent investigation that the barrier for achieving a nanosized grain structure may be broken for the Al-Zn-Mg-Cu (A-l7075) alloy by HPT possessing to an extremely high strain of $\varepsilon_{eq} \geq 1000$ which is equivalent to a rotation through 100 turns [22].

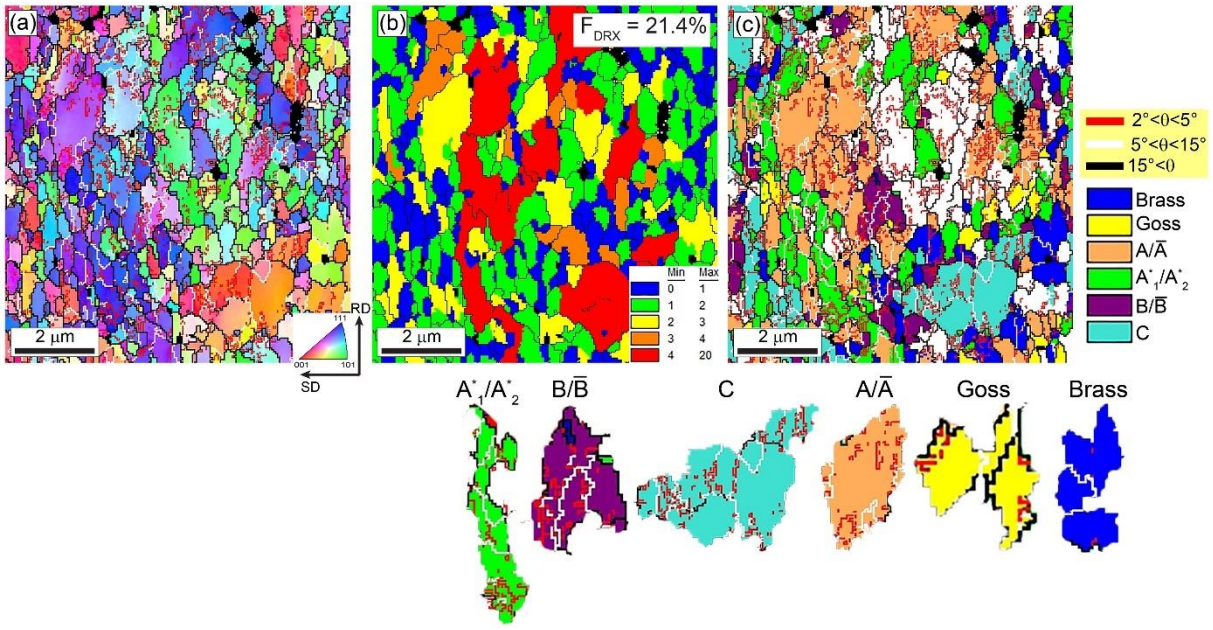

Figure 8: (a) CD-IPF map, (b) GOS map and (c) grain orientation map of selected region from a disc HPT-processed at ε_{eq} = 10.2; examples showing the shapes and the presence of different grain boundary types in A_1^*/A_2^*, $B/\bar{B}$, C, $A/\bar{A}$, Goss and Brass grains-oriented.

The development of the texture during the second grain refinement regime is very weak and the fractions of the different shear texture components are very similar as shown in Figure 5. The texture of the HPT-processed Al-based alloys usually consists at low strains of a weak *A*-fiber and a strong *B*-fiber with the dominance of the *C* component and then it becomes weaker and tends to randomize at high strains [35]. This weak texture evolution was attributed to the shear deformation nature and to the grain fragmentation. On the one hand, it is well known that shear

deformation causes a steady-state orientation flow. On the other hand, the formation of a texture gradient during the fragmentation of the parent grains will automatically create new grains with different orientations as was evident earlier in Figure 7a.

It is interesting to note that the Brass texture component exists during the shear deformation as in Figures 4 and 5. The Goss component is also present but with a lower intensity than the Brass component. It is recognized that the formation of the Goss component is an indication of the occurrence of recrystallization [48]. While the Brass component is an orientation component often developed during rolling processes in plane strain deformation, it was never reported during the HPT processing of FCC materials. The presence of the Brass component may be explained by two hypotheses based on (i) the nature of deformation loading during HPT processing and (ii) the orientation stability. Under quasi-constrained HPT processing as in the present investigation, there is a limited outflow of material between the upper and lower anvils [30, 31] and this may make the deformation essentially equivalent to plane strain deformation to thereby explain the development of the Brass and Goss texture components.

The presence of Brass through the entire equivalent strain indicates that it is a stable orientation. It was observed that the texture gradient originating from grain fragmentation was greater in unstable orientations than in stable orientations [49-51]. Thus, it can be readily seen from the orientation grain map shown in Figure 8c, which has an orientation tolerance of 20°, that the Brass oriented grains have no VLAGBs and LAGBs where this is unlike the $A/\bar{A}$, A_1^*/A_2^*, $B/\bar{B}$ and C shear-oriented grains. The Goss oriented grains also contain a smaller amount of substructure grain boundaries. The connection between the grain fragmentation and the orientation was related to the orientation symmetry and its alignment with respect to the leading direction [51, 52]. It is interesting to note that there is also a dependence of grain size on the orientation. Thus, the grain oriented A_1^*/A_2^* are more elongated than the $B/\bar{B}$ and $A/\bar{A}$ oriented grains as shown in Figure 8c. This means that the grain fragmentation and the grain size are controlled by the grain orientation.

Deformation at a strain in the range of $\varepsilon_{eq} = 4.2 - 10.2$ leads to a coarsening of the grains through a grain growth process. During this grain growth stage, the GND density remains approximately constant so that there is a balance between the dislocation generation and their annihilation. According to the available reports, the origin of the grain growth during SPD processing is not the DRX process but rather it is the shear-induced grain boundary migration [53, 54]. This indicates that the grain growth is controlled by the stress rather than by diffusion [53] and this is supported by the decrease in the DRX and the HAGBs fractions between the strains of ε_{eq} =

4.2 and 10.2 as shown in Figure 3. It must be noted also that the grain growth stage was accompanied by a strong increase in the $B/\bar{B}$ and $A/\bar{A}$ orientations leading to the domination of the *B*-fiber as in Figure 5. At this stage, the Brass component also has strength and the grain growth stage is accompanied by a decrease in the microhardness values.

Usually, the microhardness evolution of HPT-processed Al alloys follows a conventional hardening without recovery model [55] but in this model the microhardness initially increases with strain and then saturates with further strain. By contrast, the present microhardness evolution does not fully follow this model, especially in the strain range of 4.2-10.2, but eventually the microhardness in the present investigation saturated at a high strain. This saturation in the microhardness simultaneously with a saturation in the grain size and a texture stabilization.

4.2 The strengthening mechanism of the Al-6061 alloy during HPT processing

In order to realistically visualize the contribution of grain size and dislocation strengthening to the hardening behavior of the Al-6061 alloy through HPT processing, the microhardness, *Hv*, was converted to the yield strength, σ_H, following the relationship [56]:

$$\sigma_H(MPa) = 9.81\frac{Hv}{3} \quad (3)$$

The strengthening from the grain size is estimated by the Hall-Petch relationship [57, 58]:

$$\sigma_d = \frac{k_{HP}}{\sqrt{d}} \quad (4)$$

where k_{HP} is the Hall-Petch coefficient ($k_{HP} \approx 35 - 41$ Hv $\mu m^{-1/2}$ for Al [59]) and *d* is the average grain diameter.

The dislocation strengthening is measured using the Bailey–Hirsch equation [60]:

$$\sigma_\rho = \alpha' MGb\sqrt{\rho} \quad (5)$$

where $\alpha' \sim 0.24 - 0.3$ is a constant depending on the dislocation interaction, the Taylor factor is $M = 3$, *G* is the shear modulus (26 GPa for Al [61]) and ρ is the dislocation density which was obtained from KAM approach.

Figure 9 provides the yield strength, σ_H, the estimated grain size, σ_d, and dislocation strengthening, σ_ρ, for HPT discs processed at strains of ε_{eq} = 0.8, 4.2, 10.2 and 106.6, respectively.

At low stain ($\varepsilon_{eq} = 0.8$), the strengthening ($\sigma \approx 427$ MPa) is attributed to the association of grain size and dislocation strengthening ($\sigma_d + \sigma_\rho \approx 425$ MPa). This is in good agreement with the evolution of microstructure during the first grain fragmentation where there is a generation and

accumulation of dislocations and the formation of new grains through the CDRX and DDRX mechanisms.

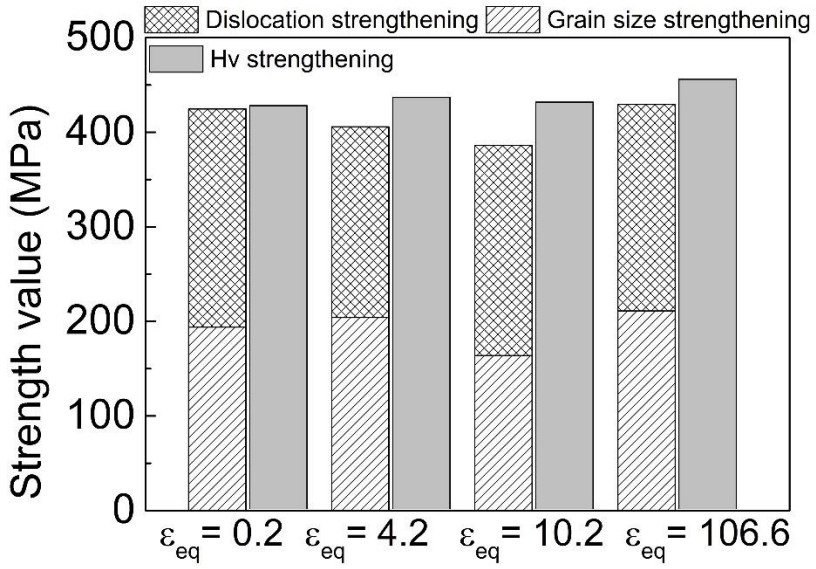

Figure 9: Yield strength, σ_H, calculated from the experimental microhardness values (Figure 6) and the estimated strengthening by grain size, σ_d, and dislocations, σ_ρ, for HPT discs processed at strains of ε_{eq} = 0.8, 4.2, 10.2 and 106.6.

The contribution of both types of strengthening decreases between strains of 4.2 and 10.2 especially for the grain size strengthening due the occurrence of grain growth within this range of strain. However, the yield strength increases to ~430 MPa at ε_{eq} = 10.2 whereas by comparison at ε_{eq} = 0.8 it is ~427 MPa indicating that additional strengthening is required. It is probable that texture strengthening may be the origin of this effect since preferred orientations of grains develop with the strengthening between strains of 4.2 and 10.2, as shown in Figures 4 and 5. The contribution of grain size increases after ε_{eq} = 106.6 and the contribution from the dislocations remains relatively stable. The summation of $\sigma_d + \sigma_\rho \approx 430$ MPa shows that grain size and dislocation strengthening are not the only contributors to the total yield strength of $\sigma \approx$ 455 MPa. It is reasonable to anticipate, therefore, that the remaining strength of ~ 25 MPa is associated with the stable weak texture formed during the steady-state period.

5. Summary and conclusions

A commercial Al-6061 alloy was processed by HPT at RT over a strain range of ε_{eq} = 0-205 using an applied pressure of 6.0 GPa. The development of the microstructure, texture and

mechanical properties of the processed discs were tracked by EBSD and Vickers microhardness measurements. Based on the experimental results, the following conclusions are reached:

- HPT processing produces a grain refinement from ~121±5 μm in the initial state to ~0.45±0.15 μm after $\varepsilon_{eq} = 205$.
- This grain refinement goes through two stages. The first stage occurs over a strain range of $\varepsilon_{eq} = 0 - 4.2$ and the second stage in the strain range of $\varepsilon_{eq} = 10.2 - 205$. There is grain growth between $\varepsilon_{eq} = 4.2$ and 10.2.
- The mechanisms of CDRX and DDRX are responsible for the grain refinement and they operate simultaneously. The grain growth stage is attributed to strain-induced grain boundary migration.
- A shear texture with the dominance of the *A*-fiber develops during the first stage of grain refinement. The texture changes to *B*-fiber with the dominance of the $B/\bar{B}$ component in the grain growth stage. Thereafter the texture becomes weak but stable during the second stage of grain refinement.
- The microhardness increases during the first grain refinement stage from 102±3 Hv to 148±2 Hv, decreases during the grain growth stage to 133±3 Hv and then increases and reaches a saturation level of 154±3 Hv in the second stage of grain refinement.
- Both grain size and dislocation strengthening contribute significantly during the first grain refinement stage and it is concluded that texture strengthening acts simultaneously with grain size and dislocation strengthening during the second grain refinement stage.

Acknowledgements

Y. Huang and T.G. Langdon were supported by the European Research Council under Grant Agreement No. 267464-SPDMETALS.

Data availability

The raw/processed data required to reproduce these findings cannot be shared at this time as the data also forms part of an ongoing study.

References

[1] S.S. Li, X. Yue, Q.Y. Li, H.L. Peng, B.X. Dong, T.S. Liu, H.Y. Yang, J. Fan, S.L. Shu, F. Qiu, Q.C. Jiang, Development and applications of aluminum alloys for aerospace industry, Journal of Materials Research and Technology 27 (2023) 944-983.
[2] E. Georgantzia, M. Gkantou, G.S. Kamaris, Aluminium alloys as structural material: A review of research, Engineering Structures 227 (2021) 111372.

[3] G. Sun, L. Zhang, B. Wen, Thermally-activated precipitation strengthening, Journal of Materials Research and Technology 29 (2024) 2131-2141.
[4] G.A. Edwards, K. Stiller, G.L. Dunlop, M.J. Couper, The precipitation sequence in Al–Mg–Si alloys, Acta Materialia 46(11) (1998) 3893-3904.
[5] M.W. Zandbergen, Q. Xu, A. Cerezo, G.D.W. Smith, Study of precipitation in Al–Mg–Si alloys by Atom Probe Tomography I. Microstructural changes as a function of ageing temperature, Acta Materialia 101 (2015) 136-148.
[6] W. Chrominski, M. Lewandowska, Precipitation strengthening of Al-Mg-Si alloy subjected to multiple accumulative roll bonding combined with a heat treatment, Materials & Design 219 (2022) 110813.
[7] C.D. Marioara, H. Nordmark, S.J. Andersen, R. Holmestad, Post-β″ phases and their influence on microstructure and hardness in 6xxx Al-Mg-Si alloys, Journal of Materials Science 41(2) (2006) 471-478.
[8] M. Werinos, H. Antrekowitsch, T. Ebner, R. Prillhofer, W.A. Curtin, P.J. Uggowitzer, S. Pogatscher, Design strategy for controlled natural aging in Al–Mg–Si alloys, Acta Materialia 118 (2016) 296-305.
[9] X. Zhang, M. Liu, H. Sun, J. Banhart, Influence of Sn on the age hardening behavior of Al–Mg–Si alloys at different temperatures, Materialia 8 (2019) 100441.
[10] G. Hillel, S. Kalabukhov, N. Frage, E. Zaretsky, L. Meshi, Direct observation of initial stages of precipitation hardening process in commercial Al 6061 alloy, Journal of Materials Science 57(22) (2022) 10395-10406.
[11] R.Z. Valiev, T.G. Langdon, Principles of equal-channel angular pressing as a processing tool for grain refinement, Progress in Materials Science 51(7) (2006) 881-981.
[12] Y. Saito, N. Tsuji, H. Utsunomiya, T. Sakai, R.G. Hong, Ultra-fine grained bulk aluminum produced by accumulative roll-bonding (ARB) process, Scripta Materialia 39(9) (1998) 1221-1227.
[13] A.P. Zhilyaev, T.G. Langdon, Using high-pressure torsion for metal processing: Fundamentals and applications, Progress in Materials Science 53(6) (2008) 893-979.
[14] R.Z. Valiev, Y. Estrin, Z. Horita, T.G. Langdon, M.J. Zehetbauer, Y. Zhu, Producing Bulk Ultrafine-Grained Materials by Severe Plastic Deformation: Ten Years Later, JOM 68(4) (2016) 1216-1226.
[15] A.P. Zhilyaev, B.K. Kim, G.V. Nurislamova, M.D. Baró, J.A. Szpunar, T.G. Langdon, Orientation imaging microscopy of ultrafine-grained nickel, Scripta Materialia 46(8) (2002) 575-580.
[16] A.P. Zhilyaev, G.V. Nurislamova, B.K. Kim, M.D. Baró, J.A. Szpunar, T.G. Langdon, Experimental parameters influencing grain refinement and microstructural evolution during high-pressure torsion, Acta Materialia 51(3) (2003) 753-765.
[17] K. Edalati, A. Bachmaier, V.A. Beloshenko, Y. Beygelzimer, V.D. Blank, W.J. Botta, K. Bryła, J. Čížek, S. Divinski, N.A. Enikeev, Y. Estrin, G. Faraji, R.B. Figueiredo, M. Fuji, T. Furuta, T. Grosdidier, J. Gubicza, A. Hohenwarter, Z. Horita, J. Huot, Y. Ikoma, M. Janeček, M. Kawasaki, P. Král, S. Kuramoto, T.G. Langdon, D.R. Leiva, V.I. Levitas, A. Mazilkin, M. Mito, H. Miyamoto, T. Nishizaki, R. Pippan, V.V. Popov, E.N. Popova, G. Purcek, O. Renk, Á. Révész, X. Sauvage, V. Sklenicka, W. Skrotzki, B.B. Straumal, S. Suwas, L.S. Toth, N. Tsuji, R.Z. Valiev, G. Wilde, M.J. Zehetbauer, X. Zhu, Nanomaterials by severe plastic deformation: review of historical developments and recent advances, Materials Research Letters 10(4) (2022) 163-256.
[18] J. Wongsa-Ngam, M. Kawasaki, T.G. Langdon, A comparison of microstructures and mechanical properties in a Cu–Zr alloy processed using different SPD techniques, Journal of Materials Science 48(13) (2013) 4653-4660.

[19] K. Edalati, Severe Plastic Deformation of Light Metals (Magnesium, Aluminum and Titanium) and Alloys by High-Pressure Torsion: Review of Fundamentals and Mechanical/Functional Properties, Materials transactions 65(5) (2024) 466-480.
[20] T.C. Lowe, R.Z. Valiev, X. Li, B.R. Ewing, Commercialization of bulk nanostructured metals and alloys, MRS Bulletin 46(3) (2021) 265-272.
[21] K. Edalati, R. Uehiro, K. Fujiwara, Y. Ikeda, H.-W. Li, X. Sauvage, R.Z. Valiev, E. Akiba, I. Tanaka, Z. Horita, Ultra-severe plastic deformation: Evolution of microstructure, phase transformation and hardness in immiscible magnesium-based systems, Materials Science and Engineering: A 701 (2017) 158-166.
[22] I.C. dos Santos, E.M. Mazzer, R.B. Figueiredo, T.G. Langdon, P.H.R. Pereira, Evidence for two-stage hardening in an Al-Zn-Mg-Cu alloy processed by high-pressure torsion, Journal of Alloys and Compounds 941 (2023) 168839.
[23] A. Loucif, R.B. Figueiredo, T. Baudin, F. Brisset, T.G. Langdon, Microstructural evolution in an Al-6061 alloy processed by high-pressure torsion, Materials Science and Engineering: A 527(18) (2010) 4864-4869.
[24] A. Loucif, R.B. Figueiredo, M. Kawasaki, T. Baudin, F. Brisset, R. Chemam, T.G. Langdon, Effect of aging on microstructural development in an Al–Mg–Si alloy processed by high-pressure torsion, Journal of Materials Science 47(22) (2012) 7815-7820.
[25] A. Loucif, R.B. Figueiredo, T. Baudin, F. Brisset, R. Chemam, T.G. Langdon, Ultrafine grains and the Hall–Petch relationship in an Al–Mg–Si alloy processed by high-pressure torsion, Materials Science and Engineering: A 532 (2012) 139-145.
[26] A. Loucif, T. Baudin, R.B. Figueiredo, F. Brisset, A.-L. Helbert, R. Chemam, T.G. Langdon, Microstructure and microtexture evolution with aging treatment in an Al–Mg–Si alloy severely deformed by HPT, Journal of Materials Science 48(13) (2013) 4573-4581.
[27] I. Fadhlina Mohamed, S. Lee, Z. Horita, Strengthening of Al 6061 Alloy by High-Pressure Torsion through Grain Refinement and Aging, Materials Science Forum 765 (2013) 408-412.
[28] I.F. Mohamed, S. Lee, K. Edalati, Z. Horita, S. Hirosawa, K. Matsuda, D. Terada, Aging Behavior of Al 6061 Alloy Processed by High-Pressure Torsion and Subsequent Aging, Metallurgical and Materials Transactions A 46(6) (2015) 2664-2673.
[29] Y. Chen, X. Yuan, J. Dong, S. Jin, G. Sha, Y. Yang, H. Zhang, C. Wang, N. Gao, M.J. Starink, The nanoscale mechanisms of strengthening and ductility enhancement in an Al–Mg–Si–Mn alloy on processing by high-pressure torsion, Materials Characterization 203 (2023) 113145.
[30] R.B. Figueiredo, P.R. Cetlin, T.G. Langdon, Using finite element modeling to examine the flow processes in quasi-constrained high-pressure torsion, Materials Science and Engineering: A 528(28) (2011) 8198-8204.
[31] R.B. Figueiredo, P.H.R. Pereira, M.T.P. Aguilar, P.R. Cetlin, T.G. Langdon, Using finite element modeling to examine the temperature distribution in quasi-constrained high-pressure torsion, Acta Materialia 60(6) (2012) 3190-3198.
[32] K. Edalati, Z. Horita, T.G. Langdon, The significance of slippage in processing by high-pressure torsion, Scripta Materialia 60(1) (2009) 9-12.
[33] P.H.R. Pereira, R.B. Figueiredo, Y. Huang, P.R. Cetlin, T.G. Langdon, Modeling the temperature rise in high-pressure torsion, Materials Science and Engineering: A 593 (2014) 185-188.
[34] K. Edalati, Y. Hashiguchi, P.H.R. Pereira, Z. Horita, T.G. Langdon, Effect of temperature rise on microstructural evolution during high-pressure torsion, Materials Science and Engineering: A 714 (2018) 167-171.
[35] H. Azzeddine, D. Bradai, T. Baudin, T.G. Langdon, Texture evolution in high-pressure torsion processing, Progress in Materials Science 125 (2022) 100886.

[36] F. Wetscher, A. Vorhauer, R. Stock, R. Pippan, Structural refinement of low alloyed steels during severe plastic deformation, Materials Science and Engineering: A 387-389 (2004) 809-816.
[37] T. Baudin, S. Bozzi, F. Brisset, H. Azzeddine, Local Microstructure and Texture Development during Friction Stir Spot of 5182 Aluminum Alloy, Crystals 13(3) (2023).
[38] M. Calcagnotto, D. Ponge, E. Demir, D. Raabe, Orientation gradients and geometrically necessary dislocations in ultrafine grained dual-phase steels studied by 2D and 3D EBSD, Materials Science and Engineering: A 527(10) (2010) 2738-2746.
[39] T. Baudin, H. Azzeddine, F. Brisset, Y. Huang, T.G. Langdon, Estimating dislocation density from electron backscatter diffraction data for an AZ31/Mg-0.6Gd hybrid alloy fabricated by high-pressure torsion, Philosophical Magazine (2024) 1-17.
[40] H. Azzeddine, Y.I. Bourezg, A.Y. Khereddine, T. Baudin, A.-L. Helbert, F. Brisset, M. Kawasaki, D. Bradai, T.G. Langdon, An investigation of the stored energy and thermal stability in a Cu–Ni–Si alloy processed by high-pressure torsion, Philosophical Magazine 100(6) (2020) 688-712.
[41] J.-H. Cho, A.D. Rollett, K.H. Oh, Determination of a mean orientation in electron backscatter diffraction measurements, Metallurgical and Materials Transactions A 36(12) (2005) 3427-3438.
[42] R. Hielscher, H. Schaeben, A novel pole figure inversion method: specification of the MTEX algorithm, Journal of Applied Crystallography 41(6) (2008) 1024-1037.
[43] O. Engler, J. Hirsch, Texture control by thermomechanical processing of AA6xxx Al–Mg–Si sheet alloys for automotive applications—a review, Materials Science and Engineering: A 336(1) (2002) 249-262.
[44] V.S. Sarma, J. Wang, W.W. Jian, A. Kauffmann, H. Conrad, J. Freudenberger, Y.T. Zhu, Role of stacking fault energy in strengthening due to cryo-deformation of FCC metals, Materials Science and Engineering: A 527(29) (2010) 7624-7630.
[45] R. Pippan, S. Scheriau, A. Taylor, M. Hafok, A. Hohenwarter, A. Bachmaier, Saturation of Fragmentation During Severe Plastic Deformation, Annual Review of Materials Research 40(1) (2010) 319-343.
[46] T. Sakai, A. Belyakov, R. Kaibyshev, H. Miura, J.J. Jonas, Dynamic and post-dynamic recrystallization under hot, cold and severe plastic deformation conditions, Progress in Materials Science 60 (2014) 130-207.
[47] A.L. Etter, S. Bozzi, T. Baudin, Dynamic Recrystallization in Similar 5182 Al/Al and Dissimilar Al/Fe Friction Stir Spot Welds, Materials Science Forum 715-716 (2012) 152-157.
[48] L. Seidel, M. Hölscher, K. Lücke, Rolling and Recrystallization Textures in Iron–3% Silicon, Textures and Microstructures 11 (1989) 197085.
[49] D. Raabe, Simulation and Experimental Examination of the Evolution of Orientation Gradients in Single Grains during Rolling of Body Centered Cubic Polycrystals, physica status solidi (b) 181(2) (1994) 291-299.
[50] L. Delannay, O.V. Mishin, D.J. Jensen, P. Van Houtte, Quantitative analysis of grain subdivision in cold rolled aluminium, Acta Materialia 49(13) (2001) 2441-2451.
[51] Y. Liu, C. Lu, H. Wang, A.K. Tieu, B. Liu, Microstructure evolution, lattice rotation retardation and grain orientation fragmentation in commercial purity aluminium deformed by high pressure torsion, Journal of Materials Research and Technology 9(3) (2020) 6642-6654.
[52] R. Quey, P.R. Dawson, J.H. Driver, Grain orientation fragmentation in hot-deformed aluminium: Experiment and simulation, Journal of the Mechanics and Physics of Solids 60(3) (2012) 509-524.
[53] K. Zhang, J.R. Weertman, J.A. Eastman, Rapid stress-driven grain coarsening in nanocrystalline Cu at ambient and cryogenic temperatures, Applied Physics Letters 87(6) (2005) 061921.

[54] Y. Liu, H. Wang, C. Lu, A. Kiet Tieu, Grain growth at fragmentation stage in commercial purity aluminium deformed by high pressure torsion, Materials Letters 277 (2020) 128272.
[55] M. Kawasaki, Different models of hardness evolution in ultrafine-grained materials processed by high-pressure torsion, Journal of Materials Science 49(1) (2014) 18-34.
[56] D. Tabor, G.I. Taylor, A simple theory of static and dynamic hardness, Proceedings of the Royal Society of London. Series A. Mathematical and Physical Sciences 192(1029) (1997) 247-274.
[57] Z.C. Cordero, B.E. Knight, C.A. Schuh, Six decades of the Hall–Petch effect – a survey of grain-size strengthening studies on pure metals, International Materials Reviews 61(8) (2016) 495-512.
[58] R.B. Figueiredo, M. Kawasaki, T.G. Langdon, Seventy years of Hall-Petch, ninety years of superplasticity and a generalized approach to the effect of grain size on flow stress, Progress in Materials Science 137 (2023) 101131.
[59] H.-J. Lee, J.-K. Han, S. Janakiraman, B. Ahn, M. Kawasaki, T.G. Langdon, Significance of grain refinement on microstructure and mechanical properties of an Al-3% Mg alloy processed by high-pressure torsion, Journal of Alloys and Compounds 686 (2016) 998-1007.
[60] J.E. Bailey, P.B. Hirsch, The dislocation distribution, flow stress, and stored energy in cold-worked polycrystalline silver, The Philosophical Magazine: A Journal of Theoretical Experimental and Applied Physics 5(53) (1960) 485-497.
[61] M. Mahmoodi, A. Naderi, Microstructure and its Relationship to Mechanical Properties in Equal Channel Angular Rolled Al6061 Alloy Sheets, Iranian Journal of Materials Forming 6(1) (2019) 16-23.